

# Measurement of Ratios of $\nu_\mu$ Charged-Current Cross Sections on C, Fe, and Pb to CH at Neutrino Energies 2–20 GeV

B.G. Tice,<sup>1,\*</sup> M. Datta,<sup>2</sup> J. Mousseau,<sup>3</sup> L. Aliaga,<sup>4,5</sup> O. Altinok,<sup>6</sup> M.G. Barrios Sazo,<sup>7</sup> M. Betancourt,<sup>8</sup> A. Bodek,<sup>9</sup> A. Bravar,<sup>10</sup> W.K. Brooks,<sup>11</sup> H. Budd,<sup>9</sup> M. J. Bustamante,<sup>5</sup> A. Butkevich,<sup>12</sup> D.A. Martinez Caicedo,<sup>13,8</sup> C.M. Castromonte,<sup>13</sup> M.E. Christy,<sup>2</sup> J. Chvojka,<sup>9</sup> H. da Motta,<sup>13</sup> J. Devan,<sup>4</sup> S.A. Dytman,<sup>14</sup> G.A. Díaz,<sup>5</sup> B. Eberly,<sup>14</sup> J. Felix,<sup>7</sup> L. Fields,<sup>15</sup> G.A. Fiorentini,<sup>13</sup> A.M. Gago,<sup>5</sup> H. Gallagher,<sup>6</sup> R. Gran,<sup>16</sup> D.A. Harris,<sup>8</sup> A. Higuera,<sup>7</sup> K. Hurtado,<sup>13,17</sup> M. Jerkins,<sup>18</sup> T. Kafka,<sup>6</sup> M. Kordosky,<sup>4</sup> S.A. Kulagin,<sup>12</sup> T. Le,<sup>1</sup> G. Maggi,<sup>11,†</sup> E. Maher,<sup>19</sup> S. Manly,<sup>9</sup> W.A. Mann,<sup>6</sup> C.M. Marshall,<sup>9</sup> C. Martin Mari,<sup>10</sup> K.S. McFarland,<sup>9,8</sup> C.L. McGivern,<sup>14</sup> A.M. McGowan,<sup>9</sup> J. Miller,<sup>11</sup> A. Mislivec,<sup>9</sup> J.G. Morfin,<sup>8</sup> T. Muhlbeier,<sup>13</sup> D. Naples,<sup>14</sup> J.K. Nelson,<sup>4</sup> A. Norrick,<sup>4</sup> J. Osta,<sup>8</sup> J.L. Palomino,<sup>13</sup> V. Paolone,<sup>14</sup> J. Park,<sup>9</sup> C.E. Patrick,<sup>15</sup> G.N. Perdue,<sup>8,9</sup> L. Rakotondravohitra,<sup>8,‡</sup> R.D. Ransome,<sup>1</sup> H. Ray,<sup>3</sup> L. Ren,<sup>14</sup> P.A. Rodrigues,<sup>9</sup> D. G. Savage,<sup>8</sup> H. Schellman,<sup>15</sup> D.W. Schmitz,<sup>20</sup> C. Simon,<sup>21</sup> F.D. Snider,<sup>8</sup> C.J. Solano Salinas,<sup>17</sup> N. Tagg,<sup>22</sup> E. Valencia,<sup>7</sup> J.P. Velásquez,<sup>5</sup> T. Walton,<sup>2</sup> J. Wolcott,<sup>9</sup> G. Zavala,<sup>7</sup> D. Zhang,<sup>4</sup> and B.P. Ziemer<sup>21</sup>

(MINERvA Collaboration)

<sup>1</sup>*Rutgers, The State University of New Jersey, Piscataway, New Jersey 08854, USA*

<sup>2</sup>*Hampton University, Dept. of Physics, Hampton, VA 23668, USA*

<sup>3</sup>*University of Florida, Department of Physics, Gainesville, FL 32611*

<sup>4</sup>*Department of Physics, College of William & Mary, Williamsburg, Virginia 23187, USA*

<sup>5</sup>*Sección Física, Departamento de Ciencias, Pontificia Universidad Católica del Perú, Apartado 1761, Lima, Perú*

<sup>6</sup>*Physics Department, Tufts University, Medford, Massachusetts 02155, USA*

<sup>7</sup>*Campus León y Campus Guanajuato, Universidad de Guanajuato, Lascruain*

*de Retana No. 5, Col. Centro. Guanajuato 36000, Guanajuato México.*

<sup>8</sup>*Fermi National Accelerator Laboratory, Batavia, Illinois 60510, USA*

<sup>9</sup>*University of Rochester, Rochester, New York 14610 USA*

<sup>10</sup>*University of Geneva, Geneva, Switzerland*

<sup>11</sup>*Departamento de Física, Universidad Técnica Federico Santa María, Avda. España 1680 Casilla 110-V, Valparaíso, Chile*

<sup>12</sup>*Institute for Nuclear Research of the Russian Academy of Sciences, 117312 Moscow, Russia*

<sup>13</sup>*Centro Brasileiro de Pesquisas Físicas, Rua Dr. Xavier Sigaud 150, Urca, Rio de Janeiro, RJ, 22290-180, Brazil*

<sup>14</sup>*Department of Physics and Astronomy, University of Pittsburgh, Pittsburgh, Pennsylvania 15260, USA*

<sup>15</sup>*Northwestern University, Evanston, Illinois 60208*

<sup>16</sup>*Department of Physics, University of Minnesota – Duluth, Duluth, Minnesota 55812, USA*

<sup>17</sup>*Universidad Nacional de Ingeniería, Apartado 31139, Lima, Perú*

<sup>18</sup>*Department of Physics, University of Texas, 1 University Station, Austin, Texas 78712, USA*

<sup>19</sup>*Massachusetts College of Liberal Arts, 375 Church Street, North Adams, MA 01247*

<sup>20</sup>*Enrico Fermi Institute, University of Chicago, Chicago, IL 60637 USA*

<sup>21</sup>*Department of Physics and Astronomy, University of California, Irvine, Irvine, California 92697-4575, USA*

<sup>22</sup>*Department of Physics, Otterbein University, 1 South Grove Street, Westerville, OH, 43081 USA*

(Dated: March 10, 2014)

We present measurements of  $\nu_\mu$  charged-current cross section ratios on carbon, iron, and lead relative to scintillator (CH) using the fine-grained MINERvA detector exposed to the NuMI neutrino beam at Fermilab. The measurements utilize events of energies  $2 < E_\nu < 20$  GeV, with  $\langle E_\nu \rangle = 8$  GeV, which have a reconstructed  $\mu^-$  scattering angle less than  $17^\circ$  to extract ratios of inclusive total cross sections as a function of neutrino energy  $E_\nu$  and flux-integrated differential cross sections with respect to the Bjorken scaling variable  $x$ . These results provide the first high-statistics direct measurements of nuclear effects in neutrino scattering using different targets in the same neutrino beam. The data are not reproduced by GENIE, a conventional neutrino-nucleus scattering simulation. Alternate models for the nuclear dependence of inelastic scattering are also considered. Measured cross section ratios exhibit a relative depletion at low  $x$  and enhancement at large  $x$  compared to all models. The observed deviations become more pronounced as the nucleon number of the target nucleus increases.

PACS numbers: 13.15.+g, 25.30.Pt, 21.10.-k

Lepton inelastic scattering is a powerful tool to probe the structure of hadrons and nuclei at small and inter-

mediate scales. The measurements of differential cross sections in charged lepton scattering experiments from

different nuclei have shown that the ratio of cross sections on a heavy nucleus to the deuteron  $\sigma^A/\sigma^D$  deviates from unity by as much as 15–20%. This demonstrates nontrivial nuclear effects over a wide region of Bjorken's dimensionless scaling variable  $x$  [1, 2]. These observations signal a difference in the quark-parton structure of a bound nucleon from that of a free nucleon and have triggered intensive theoretical exploration of background nuclear mechanisms [1, 2].

In neutrino physics, the understanding of nuclear effects is of primary importance for correct interpretation of precise measurements of electroweak parameters and evaluation of the corresponding uncertainties [3]. The need for a detailed understanding of neutrino cross sections on nuclei in order to reduce the systematic uncertainties of neutrino oscillation experiments has rekindled interest in precise measurements of these nuclear effects, albeit at lower neutrino energies where elastic and resonance processes, rather than deep inelastic processes, dominate the event sample [4].

Whereas charged lepton scattering only involves the vector current, neutrino scattering also involves the axial-vector current and is sensitive to specific quark and anti-quark flavors. For this reason, the nuclear modifications of neutrino differential cross sections may be different from those of charged leptons [5, 6]. An indirect extraction of neutrino structure function ratios using NuTeV Fe [7] and CHORUS Pb [8] data suggests quite different  $x$  behavior for neutrino compared to charged lepton scattering [9]. The latter, if confirmed, either challenges the validity of QCD factorization for processes involving bound nucleons or signals inconsistency between neutrino and charged lepton data.

Direct measurements of neutrino cross section ratios for different nuclei are therefore of significant interest and importance. So far, the only such measurements are cross section ratios of Ne to D [10], but these have large statistical uncertainties. In this Letter, we report a high statistics measurement of inclusive charged-current neutrino cross section ratios of C, Fe, and Pb to scintillator (CH) as functions of neutrino energy  $E_\nu$  and  $x$ .

MINERvA uses a finely-segmented detector to record interactions of neutrinos produced by the NuMI beamline [11] at Fermilab. The data of this analysis come from  $2.94 \times 10^{20}$  protons on target taken between March 2010 and April 2012 when the beamline was configured to produce a broadband neutrino beam peaked at 3.5 GeV and composed of  $> 95\%$   $\nu_\mu$  at the peak energy. The MINERvA detector is comprised of 120 hexagonal modules perpendicular to the  $z$ -axis, which is tilted upwards by 58 mrad with respect to the beamline [12]. There are four basic types of modules: active tracking, electromagnetic calorimeter, hadronic calorimeter, and inactive nuclear target. The most upstream part of the detector includes five inactive targets of different materials, numbered from upstream to downstream, each separated by

four active tracking modules. Target 4 is made of lead, while the other targets are composed of two or three materials arranged at differing transverse positions filling the  $x - y$  plane. Targets 1, 2, and 5 are constructed of steel and lead plates joined together; Target 3 is composed of graphite, steel, and lead. The total fiducial masses of the C, Fe, and Pb in the nuclear target region are 0.159, 0.628, and 0.711 tons, respectively. A fully active tracking region with a fiducial mass of 5.48 tons is downstream of the nuclear target region. The target and tracker regions are surrounded by electromagnetic and hadronic calorimeters. Muons used in this analysis exit the rear of the MINERvA detector and are tracked in the MINOS near detector, a magnetized iron spectrometer [13] located 2 m downstream of the MINERvA detector.

The neutrino flux is predicted using a Geant4-based simulation tuned to hadron production data [14] as described in Ref. [15]<sup>1</sup>. Neutrino interactions in the detector are simulated using the GENIE 2.6.2 neutrino event generator [16]. In GENIE, the nuclear environment is simulated by giving the initial nucleon a momentum selected from the distributions in Refs. [17, 18]. The scattering kinematics are calculated in the (off-shell) nucleon rest frame. In addition, the quasi-elastic cross section is reduced to account for Pauli blocking. For quasi-elastic and resonance processes, the free nucleon form factors are used. Details of the quasi-elastic models are given in Ref. [15]. The kinematics for non-resonant inelastic processes in GENIE are selected from the model of Ref. [19] which effectively includes target mass and higher twist corrections. An empirical correction factor based on charged lepton deep inelastic scattering measurements of  $F_2^D/F_2^{(n+p)}$  and  $F_2^{Fe}/F_2^D$  is applied to all structure functions as a function of  $x$ , independent of the four-momentum transfer squared  $Q^2$  and  $A$ . This accounts for all nuclear effects except those related to neutron excess, which are applied separately, and assumes the same nuclear effect for every nucleus heavier than deuterium.

The MINERvA detector's response is simulated by a tuned Geant4-based [20, 21] simulation. The energy scale of the detector is set by ensuring both the detected photon statistics and the reconstructed energy deposited by momentum-analyzed through-going muons agree in data and simulation. The calorimetric constants applied to reconstruct the recoil energy are determined by simulation. A cross-check of this procedure is given by comparing data and simulation of a scaled-down version of the MINERvA detector in a low energy hadron test beam [12].

Charged-current  $\nu_\mu$  events are selected by first requiring a reconstructed  $\mu^-$ . The muon is identified by a min-

<sup>1</sup> A table of the neutrino flux can be found in the Appendix.

imum ionizing track that traverses MINERvA [12] and travels downstream into the MINOS spectrometer [13] where its momentum and charge are measured. The muon selection and energy ( $E_\mu$ ) reconstruction are described in Refs. [12, 15, 22]. Requiring a matching track in MINOS significantly restricts the muon acceptance. To minimize acceptance differences across the entire MINERvA detector the analysis requires neutrino energies above 2 GeV and muon angle with respect to the beam ( $\theta_\mu$ ) less than  $17^\circ$ . A 20 GeV upper limit on neutrino energy reduces the  $\bar{\nu}_\mu$  background to  $< 1\%$ . After all selection criteria, 5953 events in C, 19024 in Fe, 23967 in Pb, and 189168 in CH are used for the analysis.

Events are associated with a nuclear target according to the position of the vertex. The event vertex is the location of the most upstream energy deposition on the muon track when only one track is reconstructed; a Kalman filter [23, 24] is used to fit the vertex position when the event has more than one track. Between 10 and 20% of selected events in the different samples have a well-reconstructed multi-track vertex; the remainder are single-track or have a poorly-reconstructed vertex position based on the  $\chi^2$  of the vertex fit. For this analysis, only events with vertices in Targets 2 through 5 and the fully active tracking volume are considered. The event sample from Target 1 has a higher background from neutrino interactions upstream of the detector.

Events that have a vertex in the active tracking region go into one of three statistically independent CH samples, which are used to form ratios with C, Fe, and Pb. Events are associated with the C, Fe, or Pb of a nuclear target if the vertex position is between one plane upstream and two planes downstream of that nuclear target module, and more than 2.5 cm away transversely from seams that join different materials in a single target. In single-track events, the muon track is propagated to the longitudinal center of the nuclear target to estimate the vertex position and momentum of the muon. After all cuts, the charged-current event selection efficiency ranges from 24% in the most upstream targets to 50% in the most downstream. The large variation in efficiencies exists because the upstream region contains more inert material and has smaller MINOS solid angle coverage.

The energy of the hadronic recoil system  $\nu$  is determined from the calorimetric sum of energy deposits not associated with the muon track. We consider only deposits which occur between 20 ns before and 35 ns after the muon (to reduce contributions from accidental overlap with other neutrino interactions) and weight their visible energies to account for the active fraction of scintillator in different regions of the detector. An overall calorimetric scale is derived by fitting calorimetrically reconstructed recoil energy to generated recoil energy for simulated events in the active tracking region [12]. Using the same procedure, additional calorimetric scales for events in Targets 2 through 5 are obtained as relative to

tracker; these are, respectively, 1.11, 1.04, 0.99, and 0.98. We identify this total reconstructed recoil energy as the energy transfer  $\nu$  used in the calculation of  $x$  below.

The kinematic variables  $E_\nu$ ,  $x$ , and  $Q^2$  for each event are obtained from the reconstructed  $E_\mu$ ,  $\theta_\mu$ , and  $\nu$ :  $E_\nu = E_\mu + \nu$ ,  $Q^2 = 4E_\nu E_\mu \sin^2(\frac{\theta_\mu}{2})$ , and  $x = \frac{Q^2}{2M_N \nu}$ , where  $M_N$  is the average of the proton and neutron masses. The reconstructed  $E_\nu$  distributions are corrected for resolution and detector smearing using an iterative Bayesian unfolding method [25] with four iterations to produce the event yields as functions of unfolded  $E_\nu$ , where the underlying generated values of  $E_\nu$  are taken from the GENIE event generator.

Reconstructed  $x$  is smeared broadly, especially at high  $x$ , where the samples are dominated by quasi-elastic processes. For these events, the hadronic recoil system can be a single nucleon, which is not reconstructed well under a calorimetric assumption. Such significant smearing would cause large uncertainties in the unfolding procedure. We therefore report cross section ratios as a function of reconstructed  $x$  and provide the migration matrices necessary to produce comparisons between theoretical models and these data in the Appendix.

The major background in the nuclear target samples is from events in adjacent tracking modules which are falsely associated with a nuclear target due to the loose cut on longitudinal vertex position. This background, referred to as “CH contamination”, ranges from 20% to 40% and is roughly proportional to the ratio of the areal density of the target to that of the surrounding scintillator. The CH contamination is determined by extrapolating the event rate measured in the active tracking region to the nuclear target region. The tracking and nuclear target regions occupy different areas, and therefore have different acceptance into the MINOS detector. Further, the presence of Fe and Pb targets in the nuclear target region stimulates greater activity in hadronic showers, which affects tracking efficiency. Events recorded in the tracking region are weighted to account for both of these differences. To account for the geometric acceptance difference, we apply a correction  $w^{t,A}(E_\mu, \theta_\mu)$ , obtained from a large, single-particle simulated  $\mu^-$  sample. Here  $t = 2, 3, 4, 5$  refers to different target numbers, and A refers to target nucleus C, Fe, or Pb. We account for efficiency differences that depend on  $\nu$  using simulated neutrino events to derive a correction  $w^{t,A}(\nu)$ . The differences are largest in the low  $\nu$  region. The acceptance and efficiency-corrected distribution is scaled such that the integrated number of events in the true background and estimated background are equal according to the neutrino event simulation. Figure 1 shows the  $x$  distribution of events passing all selection criteria in data and simulation; the predicted CH contamination is also shown.

The deviations found in simulated events between the

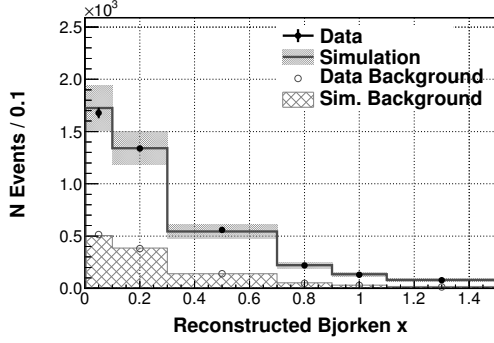


FIG. 1: Reconstructed Bjorken  $x$  distributions in data and simulation for the selected inclusive  $\nu_\mu$  events in the iron of Target 2. The plot includes CH contamination separately estimated using data and simulated events in the tracker region. Both simulation distributions are normalized to the data by the number of events passing all event selection criteria. Events are scaled to a bin size of 0.1. Events with  $x$  greater than 1.5 are not shown.

estimated CH contamination by extrapolation and the predicted CH contamination using generator-level information are not fully covered by the statistical uncertainties of the samples at the 68% confidence level in all targets. An additional systematic uncertainty is applied to ensure coverage at the 68% level. The background uncertainties consist of 2–5% from statistics and 1–8% due to systematic disagreement between estimation and prediction in the simulation.

Small backgrounds from  $\bar{\nu}_\mu$  ( $< 0.4\%$ ) and neutral current ( $< 0.1\%$ ) events are estimated using the simulation and subtracted. A background from upstream neutrino interactions of  $6.2 \pm 2.4\%$  exists only in Target 2 in one third of the data collected, because two of the modules upstream of Target 1 were not yet instrumented; the affected data are weighted accordingly. Due to transverse smearing within a single target module from one material to another, roughly 0.5% of the interactions are assigned the incorrect target nucleus; this is also estimated by simulation and subtracted.

The GENIE generator predicts a sample that is not dominated by deep inelastic scattering or any other single process. Table I shows the predicted prevalence of processes selected as a function of reconstructed  $x$ . Table II shows GENIE’s prediction for inclusive cross section ratios restricted to  $2 < E_\nu < 20$  GeV and  $\theta_\mu < 17^\circ$  with comparisons to two other models for nuclear modification of structure functions. The Kulagin-Petti microphysical model starts with neutrino-nucleon structure functions and incorporates A-dependent nuclear effects [5, 26]. The updated Bodek-Yang treatment [27] of the model implemented in GENIE [19] includes an A-dependent empirical correction based on charged lepton measurements on the nuclei of interest. Although the nuclear structure functions in the different models vary by 20%, the ratios

Reconstructed $x$	QE (%)	Res. (%)	DIS (%)	soft DIS (%)	Non-res. Inelastic Cont. (%)	Generated $Q^2$ (GeV $^2$ ) (Mean)
0.0–0.1	11.3	42.5	5.9	19.2	15.7	0.23
0.1–0.3	13.6	36.4	16.7	9.1	23.0	0.70
0.3–0.7	32.7	32.8	11.8	1.4	21.1	1.00
0.7–0.9	55.1	25.4	4.3	0.5	14.6	0.95
0.9–1.1	62.7	21.6	2.8	0.5	12.3	0.90
1.1–1.5	69.6	18.1	1.9	0.4	9.9	0.82
$> 1.5$	79.1	12.8	0.6	0.3	7.1	0.86

TABLE I: Average sample composition in different reconstructed  $x$  ranges of the selected events in nuclear targets and tracker based on GENIE simulation of different physics processes, together with the average generated  $Q^2$ . Processes are quasi-elastic (QE), baryon resonance production (Res.), deep inelastic scattering at  $Q^2 > 1$  GeV $^2$  and  $W > 2$  GeV (DIS), DIS at  $Q^2 < 1$  GeV $^2$  and  $W > 2$  GeV (soft DIS), and non-resonant inelastic continuum with  $W < 2$  GeV (Non-res. Inelastic Cont.).

$x$	C/CH				Fe/CH				Pb/CH			
	G	$\sigma_{st}$	KP	BY	G	$\sigma_{st}$	KP	BY	G	$\sigma_{st}$	KP	BY
	%	$\Delta\%$	$\Delta\%$	$\Delta\%$	%	$\Delta\%$	$\Delta\%$	$\Delta\%$	%	$\Delta\%$	$\Delta\%$	$\Delta\%$
0.0–0.1	1.050	1.0	0.3	0.0	1.011	0.5	-0.4	1.2	1.037	0.5	-1.5	0.8
0.1–0.3	1.034	0.7	-0.3	0.0	1.017	0.3	-0.7	-0.5	1.071	0.3	-1.0	-0.7
0.3–0.7	1.049	0.8	-0.1	0.0	1.049	0.4	0.0	0.0	1.146	0.4	0.4	0.6
0.7–0.9	1.089	1.8	-0.1	0.0	0.995	0.9	0.4	0.1	1.045	0.9	0.1	0.7
0.9–1.1	1.133	2.3	-0.1	0.0	0.948	1.1	0.2	0.0	0.985	1.1	0.2	0.2
1.1–1.5	1.111	2.2	0.0	0.0	0.952	1.1	0.0	0.0	1.036	1.1	0.1	0.0

TABLE II: Predictions for charged-current cross section ratios with  $2 < E_\nu < 20$  GeV and  $\theta_\mu < 17^\circ$  from GENIE (G) [19] with associated statistical uncertainty. Also shown is the deviation from GENIE predicted by the Kulagin-Petti (KP) [5, 26] and updated Bodek-Yang (BY) [27] models for nuclear modification of non-resonant inelastic events. Statistical uncertainty and deviations from GENIE are expressed as percentages. The model deviations are calculated using event reweighting, thus there are no independent statistical variations among models.

between Fe or Pb to C structure functions differ by  $\lesssim 1\%$ .

The total cross section for an  $E_\nu$  bin  $i$  is  $\sigma_i = \frac{\sum_j U_{ij}(N_j - N_j^{bg})}{\varepsilon_i T \Phi_i}$ , where  $U_{ij}$  is a matrix that accounts for smearing from true energy bin  $i$  to reconstructed energy bin  $j$ ;  $N_j$  and  $N_j^{bg}$  are the numbers of total and estimated background events in reconstructed bin  $j$ , respectively;  $\varepsilon_i$  is the efficiency for reconstructing signal events in true energy bin  $i$ ;  $T$  is the number of target nucleons; and  $\Phi_i$  is the neutrino flux in true bin  $i$ . Since unfolding is not performed in  $x$ , the flux-integrated differential cross section for a reconstructed  $x$  bin  $j$  is  $\left(\frac{d\sigma}{dx}\right)_j = \frac{N_j - N_j^{bg}}{\varepsilon_j T \Phi \Delta_j(x)}$ , where  $\Phi$  is the neutrino flux integrated from 2 to 20 GeV,  $\Delta_j(x)$  is the width of the bin, and other terms have the same meaning as above. No correction is applied to account for the neutron excess in any target nuclei.

The main sources of systematic uncertainty in the cross

$x$	I	II	III	IV	V	VI	Total
0.0–0.1	2.0	0.7	1.1	0.8	2.1	2.8	4.3
0.1–0.3	1.7	0.7	1.0	1.2	1.8	2.0	3.7
0.3–0.7	1.5	0.5	1.3	1.4	1.8	2.1	3.7
0.7–0.9	2.0	2.3	1.3	2.6	1.7	4.8	6.7
0.9–1.1	2.9	3.8	1.4	2.9	1.8	6.4	8.8
1.1–1.5	2.8	3.2	1.6	3.6	2.0	7.2	9.5

TABLE III: Systematic uncertainties (expressed as percentages) on the ratio of charged-current inclusive  $\nu_\mu$  differential cross sections  $\frac{d\sigma^{Fe}}{dx} / \frac{d\sigma^{CH}}{dx}$  with respect to  $x$  associated with (I) subtraction of CH contamination, (II) detector response to muons and hadrons, (III) neutrino interactions, (IV) final state interactions, (V) flux and target number, and (VI) statistics. The rightmost column shows the total uncertainty due to all sources.

section ratio measurements are (I) subtraction of CH contamination; (II) detector response to muon and hadrons; (III) neutrino interaction models; (IV) final state interaction models; and (V) the masses of the targets. Uncertainty in the flux is included but is negligible in the ratios of cross sections. All uncertainties are evaluated by repeating the cross section analysis with systematic shifts applied to the simulation. The sources of uncertainty in muon reconstruction are described in Ref. [15], and those from recoil energy are described in Ref. [22]. The resulting uncertainties are shown in Table III for  $\frac{d\sigma^{Fe}}{dx} / \frac{d\sigma^{CH}}{dx}$ . In general, these uncertainties are small except for the largest  $x$  bin where the interactions of the low energy hadrons produced are not as well constrained. We evaluate the systematic error from the cross section and final state interaction models by varying the underlying model tuning parameters in GENIE within their uncertainties. Since variations in model parameters also affect the calorimetric scale factors, these are re-extracted as part of the systematic error evaluation. An assay of detector components yields an uncertainty in scintillator, carbon, iron, and lead masses of 1.4%, 0.5%, 1.0%, and 0.5%, respectively.

The ratios of the charged-current  $\nu_\mu$  cross sections  $\sigma(E_\nu)$  and  $\frac{d\sigma}{dx}$  are shown in Fig. 2<sup>3</sup>. The simulation reproduces the measurements of total cross section ratios as a function of energy within roughly 10% for 1 GeV bins. In contrast, the measurements of  $\frac{d\sigma^A}{dx} / \frac{d\sigma^{CH}}{dx}$  show a suppression of the ratio compared to simulation at low  $x$  and an enhancement at high  $x$ , both of which increase with the size of the nucleus.

The low  $x$  bins are expected to show shadowing, which

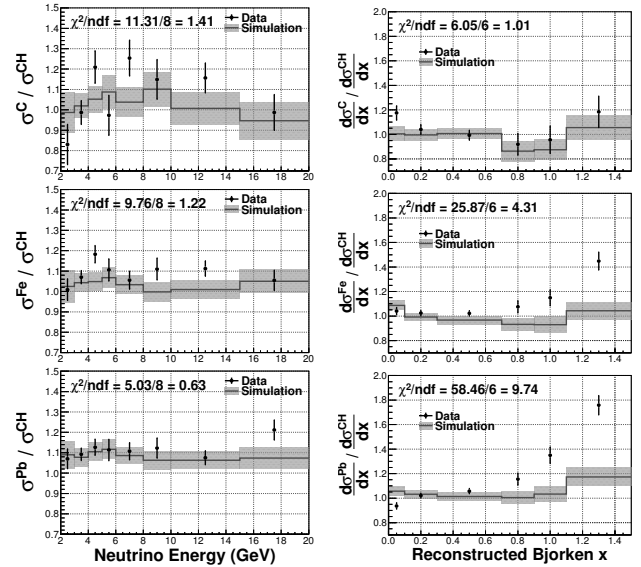


FIG. 2: Ratios of the charged-current inclusive  $\nu_\mu$  cross section as a function of  $E_\nu$  (left) and as a function of reconstructed  $x$  (right) for C/CH (top), Fe/CH (middle), and Pb/CH (bottom). Error bars on the data (simulation) show the statistical (systematic) uncertainties. The  $\chi^2$  calculation includes correlations among all bins shown. Events with  $x$  greater than 1.5 are not shown.

lowers the cross section for heavier nuclei [6, 10, 28]. Shadowing in this measurement may be larger than expected for several reasons. First, our data are at low  $Q^2$  in the non-perturbative range (80% of events below 1.0 GeV<sup>2</sup> and 60% below 0.5 GeV<sup>2</sup>), while the models are tuned to data at much higher  $Q^2$  where shadowing is well measured. Second, the shadowing effect in the model is assumed to be the same for C and Pb and equal to measurements from Fe [19]. Finally, the shadowing model used for comparison is based on charged lepton data, which do not have axial-vector contributions. The higher  $x$  bins contain mostly (>63%) quasi-elastic events, whose rates may be enhanced by meson-exchange currents [29–32], which are not included in the simulation.

The array of nuclear models available to modern neutrino experiments all give similar results for these cross section ratios, none of which are confirmed by the data. Until better models exist that cover the relevant kinematic domain, oscillation experiments need to incorporate the discrepancies measured here in evaluating systematic uncertainties in measured parameters. More theoretical work is needed to correctly model the nuclear effects in neutrino interactions, from the quasi-elastic to the deep inelastic regime.

This work was supported by the Fermi National Accelerator Laboratory under US Department of Energy contract No. DE-AC02-07CH11359 which included the MINERvA construction project. Construction support also was granted by the United States National Science

<sup>2</sup> See Supplemental Material in the Appendix for uncertainties on all cross section ratios as functions of  $E_\nu$  and  $x$ .

<sup>3</sup> See Supplemental Material in the Appendix for cross section ratio measurements compared to simulation in tabular form and correlations of uncertainties among bins.

Foundation under Award PHY-0619727 and by the University of Rochester. Support for participating scientists was provided by NSF and DOE (USA) by CAPES and CNPq (Brazil), by CoNaCyT (Mexico), by CONICYT (Chile), by CONCYTEC, DGI-PUCP and IDI/IGI-UNI (Peru), by Latin American Center for Physics (CLAF), by the Swiss National Science Foundation, and by RAS and the Russian Ministry of Education and Science (Russia). We thank the MINOS Collaboration for use of its near detector data. Finally, we thank the staff of Fermilab for support of the beamline and detector.

---

\* now at Argonne National Laboratory, Argonne, IL 60439, USA

† now at Vrije Universiteit Brussel, Pleinlaan 2, B-1050 Brussels, Belgium

‡ also at Department of Physics, University of Antananarivo, Madagascar

- [1] M. Arneodo, Phys. Rept. **240**, 301 (1994).
- [2] P. Norton, Rept. Prog. Phys. **66**, 1253 (2003).
- [3] G. P. Zeller *et al.* (NuTeV Collaboration), Phys. Rev. Lett. **88**, 091802 (2002), arXiv:0110059 [hep-ex] .
- [4] P. Coloma, P. Huber, C.-M. Jen, and C. Mariani, (2013), arXiv:1311.4506 .
- [5] S. A. Kulagin and R. Petti, Nucl. Phys. A **765**, 126 (2006), arXiv:0412425 [hep-ph] .
- [6] B. Z. Kopeliovich, J. G. Morfin, and I. Schmidt, Prog. Part. Nucl. Phys. **68**, 314 (2013), arXiv:1208.6541 [hep-ph] .
- [7] M. Tzanov *et al.* (NuTeV Collaboration), Phys. Rev. D **74**, 012008 (2006).
- [8] G. Önençüt *et al.* (CHORUS Collaboration), Phys. Lett. B **632**, 65 (2006).
- [9] K. Kovarik, I. Schienbein, F. I. Olness, J. Y. Yu, C. Kessel, J. G. Morfin, J. F. Owens, and T. Stavreva, Phys. Rev. Lett. **106**, 122301 (2011), arXiv:1012.0286 [hep-ph] .
- [10] P. Allport *et al.* (BEBC WA59 Collaboration), Physics Letters B **232**, 417 (1989).
- [11] K. Anderson *et al.*, FERMILAB-DESIGN-1998-01 (1998).
- [12] L. Aliaga *et al.* (MINERvA Collaboration), Nucl. Instrum. Methods Phys. Res., Sect. A **743**, 130 (2014), arXiv:1305.5199 [physics.ins-det] .
- [13] D. Michael *et al.* (MINOS Collaboration), Nucl. Instrum. Methods Phys. Res., Sect. A **596**, 190 (2008), arXiv:0805.3170 .
- [14] C. Alt *et al.* (NA49 Collaboration), Eur. Phys. J. C **49**, 897 (2007), arXiv:0606028 [hep-ex] .
- [15] L. Fields *et al.* (MINERvA Collaboration), Phys. Rev. Lett. **111**, 022501 (2013), arXiv:1305.2234 [hep-ex] .
- [16] C. Andreopoulos *et al.* (GENIE Collaboration), Nucl. Instrum. Methods Phys. Res., Sect. A **614**, 87 (2010), Program version 2.6.2 used here, arXiv:0905.2517 [hep-ph] .
- [17] A. Bodek and J. L. Ritchie, Phys. Rev. D **23**, 1070 (1981).
- [18] A. Bodek and J. L. Ritchie, Phys. Rev. D **24**, 1400 (1981).
- [19] A. Bodek, I. Park, and U.-K. Yang, Nucl. Phys. Proc. Suppl. **139**, 113 (2005), arXiv:0411202 [hep-ph] .
- [20] S. Agostinelli *et al.*, Nucl. Instrum. Methods Phys. Res., Sect. A **506**, 250 (2003).
- [21] J. Allison *et al.*, Nuclear Science, IEEE Transactions on **53**, 270 (2006).
- [22] G. Fiorentini *et al.* (MINERvA Collaboration), Phys. Rev. Lett. **111**, 022502 (2013), arXiv:1305.2243 [hep-ex] .
- [23] R. Frühwirth, Nucl. Instrum. Methods Phys. Res., Sect. A **262**, 444 (1987).
- [24] R. Luchsinger and C. Grab, Computer Physics Communications **76**, 263 (1993).
- [25] G. D’Agostini, Nucl. Instrum. Methods Phys. Res., Sect. A **362**, 487 (1995).
- [26] S. A. Kulagin and R. Petti, Phys. Rev. D **76**, 094023 (2007), arXiv:0703033 [hep-ph] .
- [27] A. Bodek and U. K. Yang, (2013), arXiv:1011.6592v2 .
- [28] M. Adams *et al.* (E665 Collaboration), Z. Phys. C **67**, 403 (1995), arXiv:9505006 [hep-ex] .
- [29] A. Bodek, H. S. Budd, and M. E. Christy, Eur. Phys. J. C **71**, 1726 (2011), arXiv:1106.0340 [hep-ph] .
- [30] J. E. Amaro, M. B. Barbaro, J. A. Caballero, T. W. Donnelly, and C. F. Williamson, Phys. Lett. B **696**, 151 (2011), arXiv:1010.1708 [nucl-th] .
- [31] J. Nieves, I. R. Simo, and M. J. V. Vacas, Phys. Rev. C **83**, 045501 (2011), arXiv:1102.2777 [hep-ph] .
- [32] R. Gran, J. Nieves, F. Sanchez, and M. J. V. Vacas, Phys. Rev. D **88**, 113007 (2013), arXiv:1307.8105 [hep-ph] .

## SUPPLEMENTARY MATERIAL

	$x$ Bin	Data	Sim.	$\sigma_{stat}$	$\sigma_{sys}$	$\frac{(\text{Data}-\text{Sim.})}{\sigma}$
Carbon	0.0–0.1	1.17	1.01	0.056	0.056	2.01
	0.1–0.3	1.04	1.00	0.038	0.039	0.76
	0.3–0.7	0.99	1.01	0.039	0.038	-0.25
	0.7–0.9	0.92	0.86	0.087	0.072	0.46
	0.9–1.1	0.96	0.88	0.111	0.066	0.58
	1.1–1.5	1.18	1.06	0.126	0.089	0.79
Iron	0.0–0.1	1.04	1.09	0.028	0.032	-1.02
	0.1–0.3	1.02	0.99	0.020	0.031	0.83
	0.3–0.7	1.02	0.97	0.021	0.032	1.37
	0.7–0.9	1.08	0.93	0.048	0.053	1.91
	0.9–1.1	1.15	0.93	0.064	0.075	2.14
	1.1–1.5	1.45	1.04	0.072	0.086	3.51
Lead	0.0–0.1	0.94	1.06	0.025	0.029	-2.99
	0.1–0.3	1.02	1.03	0.018	0.030	-0.32
	0.3–0.7	1.06	1.01	0.020	0.034	1.09
	0.7–0.9	1.15	1.00	0.047	0.051	2.06
	0.9–1.1	1.35	1.03	0.067	0.070	3.16
	1.1–1.5	1.76	1.17	0.077	0.103	4.45

TABLE IV: Comparison of measured values to simulation predictions for  $\frac{d\sigma^A}{dx} / \frac{d\sigma^{CH}}{dx}$  for each  $x$  bin.

	$E_\nu$ Bin (GeV)	Data	Sim.	$\sigma_{stat}$	$\sigma_{sys}$	$\frac{(\text{Data}-\text{Sim.})}{\sigma}$
Carbon	2-3	0.83	0.99	0.096	0.072	-1.23
	3-4	0.99	1.02	0.056	0.051	-0.41
	4-5	1.21	1.05	0.077	0.063	1.51
	5-6	0.97	1.09	0.096	0.058	-0.95
	6-8	1.25	1.04	0.084	0.070	1.85
	8-10	1.15	1.10	0.093	0.068	0.38
	10-15	1.16	1.01	0.069	0.075	1.36
	15-20	0.99	0.95	0.084	0.076	0.33
Iron	2-3	1.01	1.02	0.051	0.072	-0.17
	3-4	1.07	1.04	0.031	0.041	0.50
	4-5	1.18	1.05	0.041	0.043	2.17
	5-6	1.11	1.07	0.052	0.042	0.54
	6-8	1.06	1.03	0.042	0.038	0.37
	8-10	1.11	1.00	0.051	0.043	1.57
	10-15	1.11	1.01	0.035	0.043	1.73
	15-20	1.05	1.05	0.046	0.049	0.06
Lead	2-3	1.07	1.09	0.046	0.062	-0.25
	3-4	1.09	1.08	0.029	0.042	0.27
	4-5	1.13	1.10	0.038	0.042	0.37
	5-6	1.11	1.12	0.050	0.039	-0.05
	6-8	1.11	1.09	0.040	0.035	0.38
	8-10	1.12	1.06	0.047	0.039	0.91
	10-15	1.08	1.06	0.032	0.038	0.23
	15-20	1.21	1.07	0.046	0.048	1.92

TABLE V: Comparison of measured values to simulation predictions for  $\sigma^A/\sigma^{CH}$  for each  $E_\nu$  bin.

Target	Mass (ton)	Protons ( $\times 10^{30}$ )	Neutrons ( $\times 10^{30}$ )	Nucleons ( $\times 10^{30}$ )	Uncertainty %
C	0.159	0.048	0.048	0.096	1.4
Fe	0.628	0.176	0.203	0.379	0.5
Pb	0.711	0.169	0.258	0.427	1.0
CH	5.476	1.760	1.534	3.294	0.5

TABLE VI: Mass and uncertainty on mass; and number of protons, neutrons, and the total target nucleons in the fiducial volume for each nuclear target.

$E_\nu$ in Bin (GeV)	2-2.5	2.5-3	3-3.5	3.5-4	4-4.5	4.5-5	5-5.5	5.5-6	6-6.5
$\nu_\mu$ Flux (neutrinos/cm <sup>2</sup> /POT) $\times 10^{-8}$	0.409	0.501	0.526	0.419	0.253	0.137	0.080	0.055	0.042
$E_\nu$ in Bin (GeV)	6.5-7	7-7.5	7.5-8	8-8.5	8.5-9	9-9.5	9.5-10	10-11	11-12
$\nu_\mu$ Flux (neutrinos/cm <sup>2</sup> /POT) $\times 10^{-8}$	0.036	0.030	0.027	0.024	0.021	0.019	0.017	0.030	0.025
$E_\nu$ in Bin (GeV)	12-13	13-14	14-15	15-16	16-17	17-18	18-19	19-20	
$\nu_\mu$ Flux (neutrinos/cm <sup>2</sup> /POT) $\times 10^{-8}$	0.021	0.018	0.015	0.012	0.010	0.009	0.007	0.006	

TABLE VII: The calculated muon neutrino flux per proton on target (POT) for the data included in the analysis.

$x$ bin	0.0–0.1	0.1–0.3	0.3–0.7	0.7–0.9	0.9–1.1	1.1–1.5
Ratio of cross sections	1.175	1.040	0.993	0.919	0.956	1.184
Error on ratio	$\pm 0.074$	$\pm 0.054$	$\pm 0.055$	$\pm 0.110$	$\pm 0.126$	$\pm 0.149$
$x$ bin						
0.0–0.1	1.000	0.329	0.264	0.099	0.140	0.128
0.1–0.3		1.000	0.338	0.152	0.162	0.148
0.3–0.7			1.000	0.172	0.165	0.172
0.7–0.9				1.000	0.046	-0.020
0.9–1.1					1.000	0.123
1.1–1.5						1.000

TABLE VIII: Measured ratio of charged-current inclusive  $\nu_\mu$  differential cross sections  $\frac{d\sigma^C}{dx} / \frac{d\sigma^{CH}}{dx}$  with respect to  $x$ , their total (statistical and systematic) uncertainties, and the correlation matrix for these uncertainties.

$x$ bin	0.0–0.1	0.1–0.3	0.3–0.7	0.7–0.9	0.9–1.1	1.1–1.5
Ratio of cross sections	1.041	1.024	1.022	1.076	1.150	1.449
Error on ratio	$\pm 0.043$	$\pm 0.037$	$\pm 0.037$	$\pm 0.067$	$\pm 0.088$	$\pm 0.095$
$x$ bin						
0.0–0.1	1.000	0.525	0.457	0.247	0.262	0.256
0.1–0.3		1.000	0.534	0.243	0.341	0.290
0.3–0.7			1.000	0.393	0.377	0.372
0.7–0.9				1.000	0.128	0.204
0.9–1.1					1.000	0.359
1.1–1.5						1.000

TABLE IX: Measured ratio of charged-current inclusive  $\nu_\mu$  differential cross sections  $\frac{d\sigma^{Fe}}{dx} / \frac{d\sigma^{CH}}{dx}$  with respect to  $x$ , their total (statistical and systematic) uncertainties, and the correlation matrix for these uncertainties.

$x$ bin	0.0–0.1	0.1–0.3	0.3–0.7	0.7–0.9	0.9–1.1	1.1–1.5
Ratio of cross sections	0.936	1.021	1.057	1.155	1.350	1.758
Error on ratio	$\pm 0.041$	$\pm 0.035$	$\pm 0.038$	$\pm 0.065$	$\pm 0.085$	$\pm 0.103$
$x$ bin						
0.0–0.1	1.000	0.592	0.486	0.332	0.271	0.257
0.1–0.3		1.000	0.608	0.415	0.345	0.309
0.3–0.7			1.000	0.445	0.393	0.389
0.7–0.9				1.000	0.262	0.289
0.9–1.1					1.000	0.325
1.1–1.5						1.000

TABLE X: Measured ratio of charged-current inclusive  $\nu_\mu$  differential cross sections  $\frac{d\sigma^{Pb}}{dx} / \frac{d\sigma^{CH}}{dx}$  with respect to  $x$ , their total (statistical and systematic) uncertainties, and the correlation matrix for these uncertainties.

$E_\nu$ (GeV) bin	2–3	3–4	4–5	5–6	6–8	8–10	10–15	15–20
Ratio of cross sections	0.830	0.987	1.210	0.973	1.254	1.149	1.157	0.987
Error on ratio	$\pm 0.128$	$\pm 0.077$	$\pm 0.095$	$\pm 0.115$	$\pm 0.102$	$\pm 0.114$	$\pm 0.095$	$\pm 0.111$
$E_\nu$ (GeV) bin								
2–3	1.000	0.272	0.180	0.051	0.107	0.052	0.117	0.046
3–4		1.000	0.281	0.193	0.181	0.156	0.197	0.169
4–5			1.000	0.149	0.191	0.112	0.202	0.174
5–6				1.000	0.090	0.156	0.177	0.153
6–8					1.000	0.104	0.211	0.191
8–10						1.000	0.193	0.179
10–15							1.000	0.280
15–20								1.000

TABLE XI: Measured ratio of charged-current inclusive  $\nu_\mu$  total cross sections  $\sigma^C / \sigma^{CH}$  as a function of  $E_\nu$ , their total (statistical and systematic) uncertainties, and the correlation matrix for these uncertainties.

$E_\nu$ (GeV) bin	2-3	3-4	4-5	5-6	6-8	8-10	10-15	15-20
Ratio of cross sections	1.009	1.070	1.183	1.106	1.056	1.110	1.113	1.055
Error on ratio	$\pm 0.089$	$\pm 0.051$	$\pm 0.056$	$\pm 0.066$	$\pm 0.056$	$\pm 0.064$	$\pm 0.053$	$\pm 0.067$
$E_\nu$ (GeV) bin								
2-3	1.000	0.381	0.219	0.239	0.095	0.122	0.105	0.003
3-4		1.000	0.450	0.352	0.284	0.200	0.207	0.120
4-5			1.000	0.291	0.282	0.217	0.224	0.166
5-6				1.000	0.221	0.190	0.235	0.161
6-8					1.000	0.224	0.299	0.298
8-10						1.000	0.298	0.228
10-15							1.000	0.340
15-20								1.000

TABLE XII: Measured ratio of charged-current inclusive  $\nu_\mu$  total cross sections  $\sigma^{Fe}/\sigma^{CH}$  as a function of  $E_\nu$ , their total (statistical and systematic) uncertainties, and the correlation matrix for these uncertainties.

$E_\nu$ (GeV) bin	2-3	3-4	4-5	5-6	6-8	8-10	10-15	15-20
Ratio of cross sections	1.070	1.092	1.127	1.113	1.107	1.123	1.075	1.212
Error on ratio	$\pm 0.078$	$\pm 0.050$	$\pm 0.056$	$\pm 0.063$	$\pm 0.053$	$\pm 0.060$	$\pm 0.050$	$\pm 0.062$
$E_\nu$ (GeV) bin								
2-3	1.000	0.465	0.275	0.262	0.168	0.139	0.080	0.091
3-4		1.000	0.506	0.376	0.330	0.203	0.197	0.134
4-5			1.000	0.348	0.338	0.234	0.259	0.194
5-6				1.000	0.265	0.214	0.216	0.194
6-8					1.000	0.252	0.317	0.249
8-10						1.000	0.329	0.273
10-15							1.000	0.365
15-20								1.000

TABLE XIII: Measured ratio of charged-current inclusive  $\nu_\mu$  total cross sections  $\sigma^{Pb}/\sigma^{CH}$  as a function of  $E_\nu$ , their total (statistical and systematic) uncertainties, and the correlation matrix for these uncertainties.

$x$	I	II	III	IV	V	VI	Total
0.0–0.1	3.5	1.1	0.9	2.1	2.1	5.6	7.4
0.1–0.3	2.8	0.6	0.9	1.4	1.8	3.8	5.4
0.3–0.7	2.3	0.8	1.6	1.8	1.7	3.9	5.5
0.7–0.9	3.0	4.8	1.6	3.0	1.6	8.7	11.0
0.9–1.1	3.4	2.5	1.6	3.5	2.0	11.1	12.6
1.1–1.5	3.2	5.7	2.2	3.0	2.5	12.6	14.9

TABLE XIV: Systematic uncertainties (expressed as percentages) on the ratio of charged-current inclusive  $\nu_\mu$  differential cross sections  $\frac{d\sigma^C}{dx} / \frac{d\sigma^{CH}}{dx}$  with respect to  $x$  associated with (I) subtraction of CH contamination, (II) detector response to muons and hadrons, (III) neutrino interactions, (IV) final state interactions, (V) flux and target number, and (VI) statistics. The rightmost column shows the total uncertainty due to all sources.

$x$	I	II	III	IV	V	VI	Total
0.0–0.1	2.0	0.7	1.1	0.8	2.1	2.8	4.3
0.1–0.3	1.7	0.7	1.0	1.2	1.8	2.0	3.7
0.3–0.7	1.5	0.5	1.3	1.4	1.8	2.1	3.7
0.7–0.9	2.0	2.3	1.3	2.6	1.7	4.8	6.7
0.9–1.1	2.9	3.8	1.4	2.9	1.8	6.4	8.8
1.1–1.5	2.8	3.2	1.6	3.6	2.0	7.2	9.5

TABLE XV: Systematic uncertainties (expressed as percentages) on the ratio of charged-current inclusive  $\nu_\mu$  differential cross sections  $\frac{d\sigma^{Fc}}{dx} / \frac{d\sigma^{CH}}{dx}$  with respect to  $x$  associated with (I) subtraction of CH contamination, (II) detector response to muons and hadrons, (III) neutrino interactions, (IV) final state interactions, (V) flux and target number, and (VI) statistics. The rightmost column shows the total uncertainty due to all sources.

$x$	I	II	III	IV	V	VI	Total
0.0–0.1	2.2	0.7	1.0	1.1	1.8	2.5	4.1
0.1–0.3	1.9	0.7	1.1	1.1	1.6	1.8	3.5
0.3–0.7	1.6	0.7	1.5	1.6	1.6	2.0	3.8
0.7–0.9	2.5	1.5	1.5	2.5	1.7	4.7	6.5
0.9–1.1	2.6	2.5	1.6	2.8	2.1	6.7	8.5
1.1–1.5	3.0	3.5	1.9	4.2	1.9	7.7	10.3

TABLE XVI: Systematic uncertainties (expressed as percentages) on the ratio of charged-current inclusive  $\nu_\mu$  differential cross sections  $\frac{d\sigma^{Pb}}{dx} / \frac{d\sigma^{CH}}{dx}$  with respect to  $x$  associated with (I) subtraction of CH contamination, (II) detector response to muons and hadrons, (III) neutrino interactions, (IV) final state interactions, (V) flux and target number, and (VI) statistics. The rightmost column shows the total uncertainty due to all sources.

$E_\nu$ (GeV)	I	II	III	IV	V	VI	Total
2–3	3.4	5.2	4.2	2.6	3.1	9.6	12.8
3–4	3.1	1.0	2.7	2.2	2.2	5.6	7.7
4–5	3.4	1.6	2.3	2.3	2.3	7.7	9.5
5–6	4.0	3.0	2.1	1.9	2.9	9.6	11.5
6–8	3.9	2.4	1.9	1.5	2.6	8.4	10.2
8–10	4.6	2.3	2.1	1.4	3.1	9.3	11.4
10–15	5.2	1.2	1.9	2.0	2.6	6.9	9.5
15–20	5.9	1.6	1.9	1.7	2.9	8.4	11.1

TABLE XVII: Systematic uncertainties (expressed as percentages) on the ratio of charged-current inclusive  $\nu_\mu$  total cross sections  $\sigma^C / \sigma^{CH}$  as a function of  $E_\nu$  associated with (I) subtraction of CH contamination, (II) detector response to muons and hadrons, (III) neutrino interactions, (IV) final state interactions, (V) flux and target number, and (VI) statistics. The rightmost column shows the total uncertainty due to all sources.

$E_\nu$ (GeV)	I	II	III	IV	V	VI	Total
2–3	1.7	5.1	3.9	1.8	2.3	5.1	8.9
3–4	1.5	0.5	2.5	1.8	2.0	3.1	5.1
4–5	1.7	0.9	1.9	1.7	2.1	4.1	5.6
5–6	2.0	1.2	1.8	1.5	2.3	5.2	6.6
6–8	2.0	1.4	1.5	1.1	2.2	4.2	5.6
8–10	2.2	0.9	1.7	1.1	2.3	5.1	6.4
10–15	2.2	0.6	2.0	1.0	2.2	3.5	5.3
15–20	2.9	1.5	2.2	1.3	2.5	4.6	6.7

TABLE XVIII: Systematic uncertainties (expressed as percentages) on the ratio of charged-current inclusive  $\nu_\mu$  total cross sections  $\sigma^{Fe}/\sigma^{CH}$  as a function of  $E_\nu$  associated with (I) subtraction of CH contamination, (II) detector response to muons and hadrons, (III) neutrino interactions, (IV) final state interactions, (V) flux and target number, and (VI) statistics. The rightmost column shows the total uncertainty due to all sources.

$E_\nu$ (GeV)	I	II	III	IV	V	VI	Total
2–3	1.5	3.8	3.7	2.0	2.1	4.6	7.8
3–4	1.4	0.5	2.8	1.9	1.8	2.9	5.0
4–5	2.0	1.0	2.2	1.8	1.9	3.8	5.6
5–6	1.9	1.0	1.9	1.6	2.1	5.0	6.3
6–8	1.8	0.7	1.6	1.2	2.0	4.0	5.3
8–10	2.0	0.6	1.7	1.3	2.1	4.7	6.0
10–15	2.3	0.9	1.8	0.8	2.0	3.2	5.0
15–20	2.6	0.8	2.1	0.8	2.2	4.6	6.2

TABLE XIX: Systematic uncertainties (expressed as percentages) on the ratio of charged-current inclusive  $\nu_\mu$  total cross sections  $\sigma^{Pb}/\sigma^{CH}$  as a function of  $E_\nu$  associated with (I) subtraction of CH contamination, (II) detector response to muons and hadrons, (III) neutrino interactions, (IV) final state interactions, (V) flux and target number, and (VI) statistics. The rightmost column shows the total uncertainty due to all sources.

$x$ bin	0.0–0.1	0.1–0.3	0.3–0.7	0.7–0.9	0.9–1.1	1.1–1.5	overflow
0.0–0.1	73	23	3	0	0	0	0
0.1–0.3	12	60	23	2	1	1	2
0.3–0.7	4	20	47	9	5	6	9
0.7–0.9	2	11	30	11	9	10	26
0.9–1.1	2	8	30	12	6	10	31
1.1–1.5	3	7	21	8	8	14	38

TABLE XX: Fractional bin migration in variable  $x$  for the carbon sample as predicted by simulation. The value of the bin is the percent of events that were generated in an  $x$  bin (row) that were reconstructed into an  $x$  bin (column).

$x$ bin	0.0–0.1	0.1–0.3	0.3–0.7	0.7–0.9	0.9–1.1	1.1–1.5	overflow
0.0–0.1	73	23	3	0	0	0	0
0.1–0.3	12	58	23	2	1	1	2
0.3–0.7	3	18	47	10	6	6	9
0.7–0.9	2	7	31	12	9	12	27
0.9–1.1	2	6	23	12	9	15	34
1.1–1.5	2	5	16	10	9	14	44

TABLE XXI: Fractional bin migration in variable  $x$  for the iron sample as predicted by simulation. The value of the bin is the percent of events that were generated in an  $x$  bin (row) that were reconstructed into an  $x$  bin (column).

$x$ bin	0.0–0.1	0.1–0.3	0.3–0.7	0.7–0.9	0.9–1.1	1.1–1.5	overflow
0.0–0.1	72	24	4	0	0	0	0
0.1–0.3	12	59	23	2	1	1	1
0.3–0.7	3	19	47	10	6	6	9
0.7–0.9	2	8	29	13	10	12	25
0.9–1.1	2	6	23	12	11	13	33
1.1–1.5	2	5	16	11	8	14	44

TABLE XXII: Fractional bin migration in variable  $x$  for the lead sample as predicted by simulation. The value of the bin is the percent of events that were generated in an  $x$  bin (row) that were reconstructed into an  $x$  bin (column).

$x$ bin	0.0–0.1	0.1–0.3	0.3–0.7	0.7–0.9	0.9–1.1	1.1–1.5	overflow
0.0–0.1	75	22	2	0	0	0	0
0.1–0.3	10	66	21	1	1	1	1
0.3–0.7	2	15	59	11	5	4	3
0.7–0.9	2	5	33	21	14	13	12
0.9–1.1	2	4	19	19	17	19	20
1.1–1.5	1	4	12	12	14	24	33

TABLE XXIII: Fractional bin migration in variable  $x$  for the scintillator sample as predicted by simulation. The value of the bin is the percent of events that were generated in an  $x$  bin (row) that were reconstructed into an  $x$  bin (column).